Journal of Solid State Chemistry 184 (2011) 741–746

Contents lists available at ScienceDirect

Journal of Solid State Chemistry

journal homepage: www.elsevier.com/locate/jssc

$A_2TiF_5 \cdot nH_2O$ (A=K, Rb, or Cs; n=0 or 1): Synthesis, structure, characterization, and calculations of three new uni-dimensional titanium fluorides

Vinna Jo [a], Dong Woo Lee [a], Hyun-Joo Koo [b], Kang Min Ok [a,*]

[a] Department of Chemistry, Chung-Ang University, 221 Heukseok-dong, Dongjak-gu, Seoul 156-756, Republic of Korea
[b] Department of Chemistry and Research Institute for Basic Sciences, Kyung Hee University, Seoul 130-701, Republic of Korea

ARTICLE INFO

Article history:
Received 2 November 2010
Received in revised form
28 December 2010
Accepted 20 January 2011
Available online 2 February 2011

Keywords:
Synthesis
Titanium fluorides
Uni-dimensional
X-ray diffraction

ABSTRACT

Three new uni-dimensional alkali metal titanium fluoride materials, $A_2TiF_5 \cdot nH_2O$ (A=K, Rb, or Cs; n=0 or 1) have been synthesized by hydrothermal reactions. The structures of $A_2TiF_5 \cdot nH_2O$ have been determined by single-crystal X-ray diffraction. The Ti^{4+} cations have been reduced to Ti^{3+} during the synthesis reactions. All three $A_2TiF_5 \cdot nH_2O$ materials contain novel 1-D chain structures that are composed of the slightly distorted $Ti^{3+}F_6$ corner-sharing octahedra attributable to the Jahn–Teller distortion. The coordination environment of the alkali metal cations plays an important role to determine the degree of turning in the chain structures. Complete structural analyses, Infrared and UV–vis diffuse reflectance spectra, and thermal analyses are presented, as are electronic structure calculations.

1. Introduction

Transition metal fluoride materials have been studied extensively with broad interest for their important functional properties such as magnetic, electronic, multiferroic, luminescent, and storage properties [1–3]. For example, the absolute spin magnetic moment and the temperature dependence of the non-resonant magnetic intensities have been measured and studied in MF_2 (M=Mn, Fe, Co, and Ni) [3,4]. In addition, the possible coexistence of electric and magnetic ordering in tetragonal tungsten bronze (TTB) type metal fluorides such as $K_xM^{II}_xM^{III}_{1-x}F_3$, ($M$=V(II)/V(III), Fe(II)/Fe(III), Co(II)/Fe(III), Mn(II)/Fe(III), Mn(II)/Cr(III), and Mg(II)/In(III)) may make the materials potential multiferroic systems [5–10]. Meanwhile, titanium(III) fluoride materials are of significant interest attributed to their structural and optical properties originated from the d^1 electronic configuration of Ti^{3+} [11–15]. Thus, to understand the structural basis of the coordination environments around the Ti^{3+} would be very important, as these environments are one of the major factors that influence on the materials' electronic properties. Titanium(III) fluoride materials are normally synthesized through standard solid-state reaction techniques [11–15], hydrothermal methods [16], and high pressure synthesis methods [17]. Among them, hydrothermal reaction techniques for the synthesis of new titanium(III) fluoride materials have the virtue of providing for a variety of structural motifs under relatively mild reaction conditions. In hydrothermal synthetic method, mineralizers in the form of acids or bases are often introduced to increase the solubility of the sparingly soluble reagents [18,19]. Besides, organic or inorganic structure-directing agents influence profoundly on the formation of various framework structures and their subsequent physical properties [20–22]. In this paper, we report three new uni-dimensional titanium(III) fluoride materials, $A_2TiF_5 \cdot nH_2O$ (A=K, Rb, or Cs; n=0 or 1). With the three materials, we are going to explore the reduction of the Ti^{4+} to Ti^{3+} during the hydrothermal synthesis reactions. Complete structural analyses by X-ray diffraction, Infrared and UV–vis diffuse reflectance spectra, thermal analyses, and electronic structure calculations on the materials were performed.

2. Experimental

2.1. Reagents

TiO_2 (Kanto, 99.5%), KHF_2 (Aldrich, 99%), RbF (Aldrich, 99.8%), CsF (Aldrich, 99%), and N,N-Dimethylformamide (Aldrich, 99.8%) were used as received.

2.2. Synthesis

Single crystals of β-K_2TiF_5, $Rb_2TiF_5 \cdot H_2O$, and $Cs_2TiF_5 \cdot H_2O$ were synthesized by a hydrothermal reaction method. For β-K_2TiF_5, 0.240 g (3.00×10^{-3} mol) of TiO_2 and 0.780 g (1.00×10^{-2} mol) of

* Corresponding author. Fax: +82 2 825 4736.
E-mail address: kmok@cau.ac.kr (K.M. Ok).

0022-4596/$ - see front matter © 2011 Elsevier Inc. All rights reserved.
doi:10.1016/j.jssc.2011.01.029

KHF_2 were combined with 0.9 mL of DMF and 4.0 mL of H_2O. For $Rb_2TiF_5 \cdot H_2O$, 0.120 g (1.50×10^{-3} mol) of TiO_2 and 1.567 g (1.50×10^{-2} mol) of RbF were combined with 1.0 mL of DMF and 4.0 mL of H_2O. For $Cs_2TiF_5 \cdot H_2O$, 0.217 g (1.50×10^{-3} mol) of Ti_2O_3 and 1.519 g (1.50×10^{-2} mol) of CsF were combined with 0.9 mL of DMF and 4.0 mL of H_2O. The respective reactants were transferred to Teflon-lined stainless steel autoclaves. The autoclaves were subsequently sealed and heated to 230 °C at 1 °C min^{-1}, held for 72 h, and cooled to room temperature at a rate of 6 °C h^{-1}. The products were recovered by filtration, washed with water, and allowed to dry in air. Light violet single crystals of β-K_2TiF_5, $Rb_2TiF_5 \cdot H_2O$, and $Cs_2TiF_5 \cdot H_2O$ were recovered in 82%, 85%, and 86% yields, respectively, based on the titanium oxide. Powder X-ray diffraction patterns on the synthesized phases are in good agreement with the generated patterns from the single-crystal data (see the Supporting Information).

2.3. Single crystal X-ray diffraction

Light violet rods (β-K_2TiF_5: $0.06 \times 0.08 \times 0.26$ mm^3, $Rb_2TiF_5 \cdot H_2O$: $0.04 \times 0.06 \times 0.22 mm^3$, $Cs_2TiF_5 \cdot H_2O$: $0.04 \times 0.06 \times 0.20$ mm^3) were used for single crystal data analyses. All of the data were collected using a Bruker SMART APEX diffractometer equipped with a 1 K CCD area detector using graphite monochromated Mo $K\alpha$ radiation at room temperature at the Korea Basic Science Institute. A hemisphere of data was collected using a narrow-frame method with scan widths of 0.30° in omega, and an exposure time of 5 s/frame. The first 50 frames were remeasured at the end of the data collection to monitor instrument and crystal stability. The maximum correction applied to the intensities was $< 1\%$. The data were integrated using the SAINT program [23], with the intensities corrected for the Lorentz, polarization, air absorption, and absorption attributable to the variation in the path length through the detector faceplate. A semiempirical absorption correction was made on the hemisphere of data with the SADABS program [24]. The data were solved and refined using SHELXS-97 and SHELXL-97, respectively [25,26]. All of the atoms were refined with anisotropic thermal parameters and converged for $I > 2\sigma(I)$. All calculations were performed using the WinGX-98 crystallographic software package [27]. Crystallographic data and selected bond distances for the reported materials are given in Tables 1 and 2.

2.4. Powder X-ray diffraction

Powder X-ray diffraction was used to confirm the phase purity for each sample. The X-ray powder diffraction data were collected on a Scintag XDS2000 diffractometer at room temperature (Cu $K\alpha$ radiation, $\theta - \theta$ mode, flat plate geometry) equipped with Peltier germanium solid state detector in the 2θ range 5–70° with a step size of 0.02°, and a step time of 1 s.

2.5. Infrared spectroscopy

Infrared spectra were recorded on a Varian 1000 FT-IR spectrometer in the 400–4000 cm^{-1} range, with the samples intimately pressed between two KBr pellets.

2.6. UV–vis diffuse reflectance spectroscopy

UV-visible reflectance data were collected on a Varian Cary 500 scan UV–vis-NIR spectrophotometer over the spectral range $200 - 1500$ nm at room temperature. Poly(tetrafluoroethylene) was used as a reference material. Reflectance spectrum was converted to the absorbance using the Kubelka–Munk function [28,29].

Table 1
Crystallographic data for β-K_2TiF_5, $Rb_2TiF_5 \cdot H_2O$, and $Cs_2TiF_5 \cdot H_2O$.

Empirical formula	β-K_2TiF_5	$Rb_2TiF_5 \cdot H_2O$	$Cs_2TiF_5 \cdot H_2O$
Formula weight	221.10	331.86	426.74
Crystal system	Orthorhombic	Orthorhombic	Orthorhombic
Space group	*Pnma* (No. 62)	*Cmcm* (No. 63)	*Cmcm* (No. 63)
a (Å)	5.9550(12)	9.6450(19)	10.266(2)
b (Å)	7.4170(15)	8.4731(17)	8.7772(18)
c (Å)	10.718(2)	7.8623(16)	8.0150(16)
V (Å^3)	473.40(16)	642.5(2)	722.2(3)
Z	4	4	4
Temperature (K)	298.0(2)	298.0(2)	298.0(2)
ρ_{calcd} (g cm^{-3})	3.102	3.431	3.925
μ (mm^{-1})	3.564	16.405	11.138
Crystal color	Light violet	Light violet	Light violet
Crystal habit	Rod	Rod	Rod
Crystal size (mm^3)	$0.06 \times 0.08 \times 0.26$	$0.04 \times 0.06 \times 0.22$	$0.04 \times 0.06 \times 0.20$
Reflections collected	2439	2436	2547
Independent reflections	444	519	548
R(int)	0.0267	0.0304	0.0272
T_{min}, T_{max}	0.72, 0.81	0.32, 0.52	0.45, 0.64
No. of parameters	46	31	31
Goodness-of-fit on F^2	1.193	1.239	1.241
X-ray radiation (λ, Å)	Mo $K\alpha$ (0.71073)		
θ range (deg.)	3.34 – 24.99	3.20 – 30.02	3.05 – 30.02
Limiting indices	$-7 \le h \le 7$, $-8 \le k \le 8$, $-8 \le l \le 12$	$-13 \le h \le 9$, $-11 \le k \le 9$, $-11 \le l \le 11$	$-14 \le h \le 8$, $-12 \le k \le 12$, $-11 \le l \le 11$
Refinement method	Full-matrix least-squares on F^2 [SHELXL-97]		
$R(F)$[a]	0.0572	0.0385	0.0374
$R_w(F_0^2)$[b]	0.1653	0.0807	0.1108
Largest diff. peak and hole (e Å^{-3})	0.527 and −2.449	−1.819 and 1.991	−2.744 and 2.277

[a] $R(F) = \Sigma \| F_0 | - | F_c \| / \Sigma | F_0 |$.
[b] $R_w(F_0^2) = [\Sigma w(F_0^2 - F_c^2)^2 / \Sigma w(F_0^2)^2]^{1/2}$.

Table 2
Selected bond distances (Å) for β-K_2TiF_5, $Rb_2TiF_5 \cdot H_2O$, and $Cs_2TiF_5 \cdot H_2O$

β-K_2TiF_5			
Ti(1)–F(1) × 2	1.876(4)	Ti(1)–F(2) × 2	1.884(4)
Ti(1)–F(3) × 2	1.928(2)		
$Rb_2TiF_5 \cdot H_2O$			
Ti(1)–F(1) × 2	1.899(7)	Ti(1)–F(2) × 2	1.909(7)
Ti(1)–F(3) × 2	1.9671(7)		
$Cs_2TiF_5 \cdot H_2O$			
Ti(1)–F(1) × 2	1.886(10)	Ti(1)–F(2) × 2	1.915(7)
Ti(1)–F(3) × 2	2.0056(9)		

2.7. Thermogravimetric analysis (TGA)

Thermogravimetric analysis was performed on a Setaram LABSYS TG–DTA/DSC Thermogravimetric Analyzer. The polycrystalline β-K_2TiF_5, $Rb_2TiF_5 \cdot H_2O$, and $Cs_2TiF_5 \cdot H_2O$ samples were contained within alumina crucibles and heated at a rate of 10 °C min^{-1} from room temperature to 800 °C under flowing argon.

2.8. Scanning electron microscope/energy dispersive analysis by X-ray (SEM/EDAX)

SEM/EDAX analyses have been performed using a Hitachi S-3400 N/Horiba Energy EX-250 instruments. EDAX for β-K_2TiF_5,$Rb_2TiF_5 \cdot H_2O$, and $Cs_2TiF_5 \cdot H_2O$ reveal a K (Rb or Cs)/Ti ratio of approximately 2:1.

2.9. Theoretical calculations

First principles density functional theory (DFT) calculations were carried out using the frozen core projector augmented wave (PAW) method [30] encoded in the Vienna ab initio simulation package (VASP) [31] with the generalized gradient approximation (GGA) [32] for the exchange and correlation correction. Our spin-polarized DFT calculations employed the plane wave cutoff energy of 450 eV, the sampling of the irreducible Brillouin zone with $12\times6\times8$ points, and the total energy convergence threshold of 10^{-6} eV.

3. Results and discussion

3.1. Syntheses

The reactions of TiO_2 and KHF_2 or RbF under hydrothermal reaction conditions with small amount of DMF result in the formation of β-K_2TiF_5 or $Rb_2TiF_5\cdot H_2O$, respectively. One can notice that the starting Ti^{4+} cations have been reduced to Ti^{3+} during the reactions for both materials. It has been known that DMF can act as a reducing agent under suitable conditions [33]. The possible reduction process may involve the following reaction:

$$HCONMe_2+2Ti^{4+}+H_2O\rightarrow Me_2NCOOH+2Ti^{3+}+2H^+$$

It has been also reported that the reduction rate would greatly increase at higher temperature with the decomposition of carbamic acid to CO_2 and Me_2NH [34]. This similar reduction process of Ti^{4+} to Ti^{3+} during the hydrothermal reaction has been observed before as well [16]. β-K_2TiF_5 and $Rb_2TiF_5\cdot H_2O$ were produced as moderate-sized, light violet rod crystals. Crystals of β-K_2TiF_5 and $Rb_2TiF_5\cdot H_2O$ were also successfully obtained from the reactions of TiF_3 (or Ti_2O_3), KF (or RbF), and H_2O at 230 °C, which clearly confirm the oxidation state of titanium (Ti^{3+}) in the products and reducing ability of DMF. We were also able to synthesize pure crystals of $Cs_2TiF_5\cdot H_2O$ directly from the reaction between Ti_2O_3 and CsF under the same reaction condition.

3.2. Structures

All three materials β-K_2TiF_5, $Rb_2TiF_5\cdot H_2O$, and $Cs_2TiF_5\cdot H_2O$ are new ternary $A^+-Ti^{3+}-$fluorides containing Ti–F–Ti bonds. While β-K_2TiF_5 crystallizes in an orthorhombic space group *Pnma* (No. 62) that are isostructural to $(NH_4)_2MF_5$ (M=Mn or Ti) [16,35], $Rb_2TiF_5\cdot H_2O$ and $Cs_2TiF_5\cdot H_2O$ exhibit a new space group *Cmcm* (No. 63). However, they do have similar structures consisting of chains of TiF_6 octahedra and K^+, Rb^+, or Cs^+ alkali metal cations. The unique Ti^{3+} cation is linked to six fluorine atoms in distorted octahedral environment. Bond distances of TiF_6 octahedra range 1.8745(17)–1.9274(9), 1.899(7)–1.9671(7), and 1.886(10)–2.0056(9) Å for β-K_2TiF_5, $Rb_2TiF_5\cdot H_2O$, and $Cs_2TiF_5\cdot H_2O$, respectively. Interestingly, for all three materials, distortions in the Ti-centered octahedra occurred and resulted in bond asymmetries within the TiF_6 octahedra; while four normal Ti–F bonds are observed in the equatorial position, two longer Ti–F bonds are observed in the axial position (see Fig. 1 and Table 2). Specifically, the two longer Ti–F bonds in each TiF_6 octahedron are observed from the Ti(1)–F(3) bonds that are aligned along the corner-sharing octahedral chains for all three reported materials. As we will discuss in detail later, the bond asymmetries in the TiF_6 octahedra are attributable to the Jahn–Teller distortion [36]. The F–Ti–F bond angles range 89.43(10)–180°, 89.4(5)–180°, and 89.7(6)–180.0(11)° for β-K_2TiF_5, $Rb_2TiF_5\cdot H_2O$, and $Cs_2TiF_5\cdot H_2O$, respectively. These bond distances and angles are consistent with those of previously reported titanium fluorides [13–16]. The K–F, Rb–F, or Cs–F contacts range 2.7074(18)–3.100(4) Å for β-K_2TiF_5, 2.815(2)–3.347(5) Å for $Rb_2TiF_5\cdot H_2O$, and 2.948(4)–3.542(10) Å for $Cs_2TiF_5\cdot H_2O$. Each fluorine atom is bonded to Ti^{3+} cation. Thus in connectivity terms, the structures may be written as infinite anionic chains of $[Ti^{3+}F_{2/2}F_{4/1}]^{2-}$ with charge balance maintained by the two A^+ (A=K, Rb, or Cs) cations. Bond valence calculations [37,38] resulted in values of 0.92–1.02 for K^+ and 2.89 for Ti^{3+} in β-K_2TiF_5, 0.93 for Rb^+ and 2.73 for Ti^{3+} in $Rb_2TiF_5\cdot H_2O$, and 1.05 for Cs^+ and 3.18 for Ti^{3+} in $Cs_2TiF_5\cdot H_2O$.

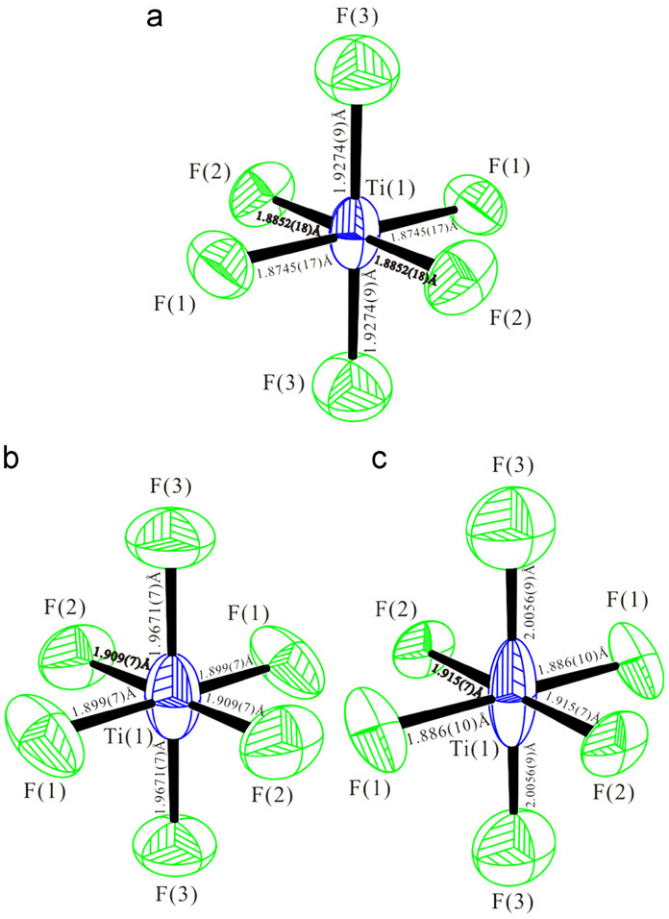

Fig. 1. ORTEP (90% probability ellipsoids) for $Ti^{3+}F_6$ octahedra in (a) β-K_2TiF_5, (b) $Rb_2TiF_5\cdot H_2O$, and (c) $Cs_2TiF_5\cdot H_2O$.

The distorted TiF_6 octahedra are linked through F(3) along the [0 1 0] for β-K_2TiF_5 and along the [0 0 1] for $Rb_2TiF_5\cdot H_2O$ and $Cs_2TiF_5\cdot H_2O$ (see Fig. 2). The linkages produce infinite uni-dimensional parallel chains of corner-sharing TiF_6 octahedra. The alkali metal cations, K^+, Rb^+, or Cs^+ reside within the crystal lattice and maintain charge balances. As can be seen in Fig. 2, the TiF_6 octahedral chains in β-K_2TiF_5 run "zigzag" along the *b*-direction. However, those chains for $Rb_2TiF_5\cdot H_2O$ and $Cs_2TiF_5\cdot H_2O$ exhibit only very slight turns. The difference may be attributed to the coordination environment of alkali metal cations. Because of the ionic size of K^+, relatively small coordination environments are preferred. Thus, in β-K_2TiF_5, the two unique K^+ cations are in KF_9 and KF_{10} coordination environments and the interaction between K^+ cations and the fluorine ligands are substantial (see Fig. 3(a)). To achieve this coordination environment around each of the K^+, the TiF_6 octahedral chains in β-K_2TiF_5 must be aligned in a zigzag manner. On the other hand, the larger ionic sizes of Rb^+ and Cs^+ require larger coordination environments. Thus, the Rb^+ and Cs^+ cations are in twelve-fold coordination environments, $AF_{10}(OH_2)_2$, in $Rb_2TiF_5\cdot H_2O$ and $Cs_2TiF_5\cdot H_2O$ (see Fig. 3(b)). This larger

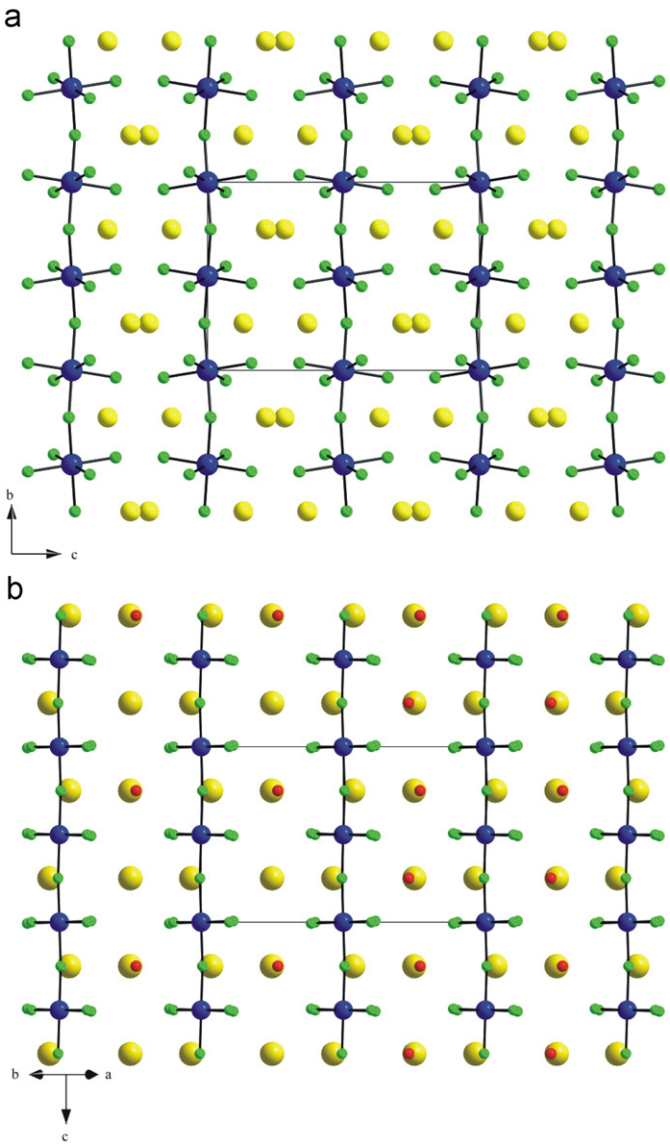

Fig. 2. Ball-and-stick diagrams of (a) β-K_2TiF_5 and (b) $Rb_2TiF_5 \cdot H_2O$ or $Cs_2TiF_5 \cdot H_2O$ (blue, Ti; green, F; red, O; yellow, K, Rb, or Cs). Note the TiF_6 octahedra are linked along the [0 1 0] for β-K_2TiF_5 and along the [0 0 1] for $Rb_2TiF_5 \cdot H_2O$ or $Cs_2TiF_5 \cdot H_2O$. All three reported materials exhibit infinite unidimensional chain structures. (For interpretation of the references to color in this figure legend, the reader is referred to the web version of this article.)

coordination environment of Rb^+ or Cs^+ makes the TiF_6 octahedra turn in a weak manner along the chains. With the $Rb_2TiF_5 \cdot H_2O$ and $Cs_2TiF_5 \cdot H_2O$, water molecules are residing in the crystal lattice as well. Thus, we observe that hydrogen bonds occur from the terminal fluorine atom [F(2)] in the TiF_6 octahedra to the oxygen atom in the water molecule [F(2)···O(w1) 2.754(12) and 2.744(16) Å for $Rb_2TiF_5 \cdot H_2O$ and $Cs_2TiF_5 \cdot H_2O$, respectively]. We must point out that a polymorph of α-K_2TiF_5 synthesized under high pressure has been recently reported [17]. Although α-K_2TiF_5 shares a 1D chain structural motif, the TiF_6 octahedra in α-K_2TiF_5 are *cis*-corner-connected along the *c*-axis. However, all the TiF_6 octahedra reported here are the *trans*-corner-connected to form infinite chains.

3.3. Infrared spectroscopy

The infrared spectra of β-K_2TiF_5, $Rb_2TiF_5 \cdot H_2O$, and $Cs_2TiF_5 \cdot H_2O$ revealed Ti – F vibrations in the region *ca.* 523 – 562 cm^{-1}. With the $Rb_2TiF_5 \cdot H_2O$ and $Cs_2TiF_5 \cdot H_2O$, O – H vibrations are also observed around 3460 and 1660 cm^{-1}. The assignments are consistent with those previously reported [39,40].

3.4. UV–vis diffuse reflectance spectroscopy

UV–vis diffuse reflectance spectra were collected on the β-K_2TiF_5 and $Rb_2TiF_5 \cdot H_2O$ (see the Supporting Information). Absorption (*K*/*S*) data were calculated from the following Kubelka–Munk function [28,29]:

$$F(R) = \frac{(1-R)^2}{2R} = \frac{K}{S}$$

where *R* is the reflectance, *K* the absorption, and *S* the scattering. In the (*K*/*S*)-versus-*E* plot, extrapolating the linear part of the rising curve to zero provided the onset of absorption at ~3.8 and 3.5 eV for β-K_2TiF_5 and $Rb_2TiF_5 \cdot H_2O$, respectively. Close examination of the UV–vis diffuse reflectance spectra for both materials shows that β-K_2TiF_5 and $Rb_2TiF_5 \cdot H_2O$ exhibit two overlapping broad absorption bands around 557 and 566 nm, respectively, which is attributable to the Jahn–Teller distortions of the $Ti^{3+}F_6$ octahedra [36]. For the d^1 complexes with weak field ligands such as F, the e_g orbitals can split into two of slightly different energy in its excited state through the Jahn–Teller distortion. Thus, excitation can occur from the asymmetrically occupied t_{2g} level to either of the excited states of slightly different energy, which result in a broadening of the electronic spectra. Structurally the distortion often occurs in the form of an elongation or compression along an axis to reduce the degeneracy. As described in the

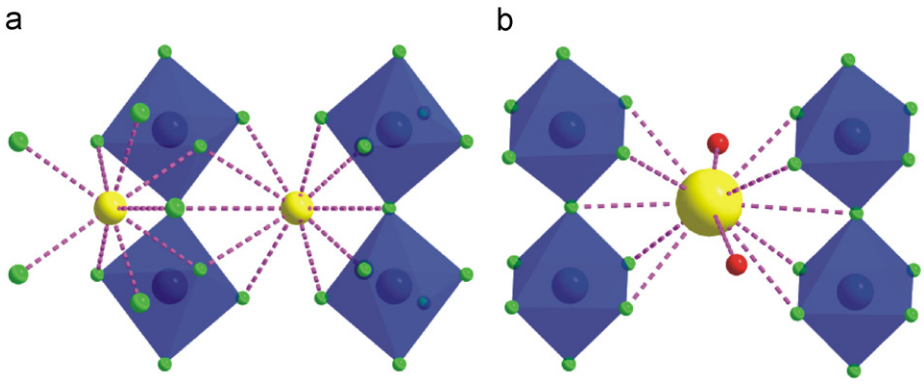

Fig. 3. Ball-and-stick and polyhedral representations for (a) β-K_2TiF_5 and (b) $Rb_2TiF_5 \cdot H_2O$ or $Cs_2TiF_5 \cdot H_2O$ with the K^+ and Rb^+ (or Cs^+) coordination environment emphasized.

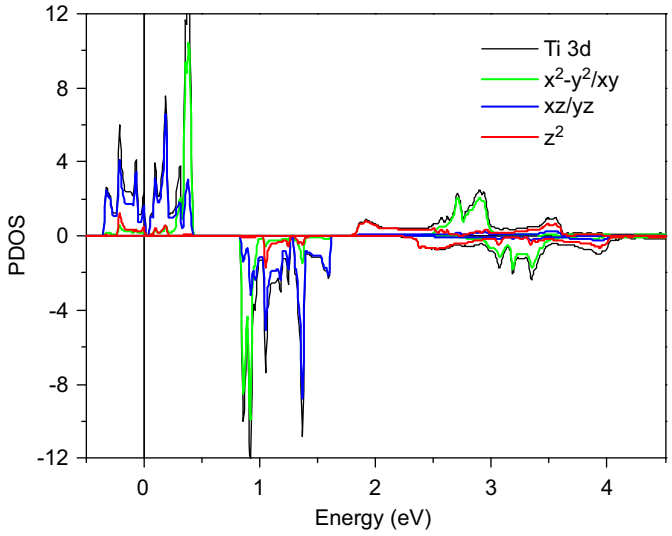

Fig. 4. The partial DOS plot of β-K_2TiF_5 obtained from spin-polarized GGA calculations. The solid line indicates Fermi level.

structure section, all three reported materials reveal two long Ti−F bonds within TiF_6 octahedra along an axis, which is consistent with the result of the Jahn–Teller distortion.

3.5. Thermal analysis

The thermal behaviors of β-K_2TiF_5, $Rb_2TiF_5 \cdot H_2O$, and $Cs_2TiF_5 \cdot H_2O$ were investigated using thermogravimetric analysis. TGA measurement on polycrystalline sample of β-K_2TiF_5 revealed that the material was stable up to 540 °C. After that the material started decomposing, which possibly is attributed to the loss of fluorides. It was not possible to analyze the final product with powder XRD, since a very small amount of the residue was stuck to the alumina crucible at such a high temperature. With the $Rb_2TiF_5 \cdot H_2O$ and $Cs_2TiF_5 \cdot H_2O$, weight losses of 5.09% and 3.96% are observed between 120 and 180 °C, respectively, which are attributable to the loss of the occluded water molecule from the materials. No dramatic peak changes have been observed in the powder XRD patterns after removal of the occluded water molecules from the materials. It is not surprising we do not see any significant changes in the framework chains, since the interactions between the larger cations, Rb^+ (or Cs^+) with the fluoride ligands in the TiF_6 octahedra would be almost same. Also the loss of occluded water from $Rb_2TiF_5 \cdot H_2O$ and $Cs_2TiF_5 \cdot H_2O$ is reversible; if the dehydrated materials are immersed in water, complete rehydration occurs within a few hours. Both $Rb_2TiF_5 \cdot H_2O$ and $Cs_2TiF_5 \cdot H_2O$ are stable up to approximately 800 °C. The TGA curves for the reported materials have been deposited in the Supporting Information.

3.6. Electronic structure calculations

The partial density of states (PDOS) plot is obtained by performing spin-polarized GGA calculations for β-K_2TiF_5 is shown in Fig. 4. The bottom of the band from approximately −0.35–0.4 eV is predominantly contributed by the up-spin Ti t_{2g} orbitals and the top part approximately from 2.0 to 3.5 eV mainly consists of the up-spin Ti e_g orbitals. The up-spin Ti t_{2g} block bands are partially filled (i.e. approximately one-third of the total accommodation of the up-spin Ti t_{2g} bands), while the down-spin Ti t_{2g} block is totally empty. This fact indicates the presence of Ti^{3+} in β-K_2TiF_5. The PDOS of t_{2g} bands consists of two dispersive bands and one narrow band due to the local TiF_6 symmetry made up of the three nonequivalent Ti−F bonds and the one-dimensional characteristic of β-K_2TiF_5. In addition, the PDOS has an energy split between the t_{2g} and e_g-blocks, which is similar to the result from that of UV–vis diffuse reflectance spectra attributable to the Jahn–Teller distortions of the $Ti^{3+}F_6$ octahedra.

4. Conclusions

We have demonstrated that three new uni-dimensional alkali metal titanium fluoride materials, $A_2TiF_5 \cdot nH_2O$ (A=K, Rb, or Cs; n=0 or 1) were successfully synthesized through hydrothermal reactions. The materials have been structurally characterized by single-crystal and powder diffraction. All three $A_2TiF_5 \cdot nH_2O$ materials exhibit novel 1-D chain structures consisting of the slightly distorted $Ti^{3+}F_6$ corner-sharing octahedra attributed to the Jahn–Teller distortion. Further full characterization including infrared and UV–vis diffuse reflectance spectra, thermal analysis, and electronic structure calculations have been thoroughly performed.

Acknowledgments

This research was supported by Basic Science Research Program through the National Research Foundation of Korea (NRF) funded by Ministry of Education, Science & Technology (grant: 2010-0002480). H.-J. Koo thanks the Korean Research Foundation (Grant KRF-2007-C00028; MOEHRD, Basic Research Promotion Fund).

Appendix A. Supplementary materials

Supplementary materials associated with this article can be found in the online version at doi:10.1016/j.jssc.2011.01.029.

Calculated and observed X-ray diffraction patterns, Infrared spectra, UV–vis diffuse reflectance spectra, and thermogravimetric analysis diagrams are available (PDF).

References

[1] S. Fabbrici, E. Montanari, L. Righi, G. Calestani, A. Migliori, Chem. Mater. 16 (2004) 3007.
[2] H. Li, P. Balaya, J. Maier, J. Electrochem. Soc. 151 (2004) A1878.
[3] J. Strempfer, U. Rutt, S.P. Bayrakci, T. Bruckel, W. Jauch, Phys. Rev. B: Condens. Matter 69 (2004) 014417/1.
[4] J. Strempfer, U. Rutt, W. Jauch, Phys. Rev. Lett. 86 (2001) 3152.
[5] R. De Pape, C. R. Acad. Sci. Paris 260 (1965) 4527.
[6] R.F. Williamson, W.O. Boo, J. Inorg. Chem. 16 (1977) 649.
[7] E. Banks, S. Nakajima, G.J.B. Williams, Acta Crystallogr., Sect. B: Struct. Sci. 35 (1979) 46.
[8] E. Banks, M. Shone, Y.S. Hong, R.F. Williamson, W.O. Boo, J. Inorg. Chem. 21 (1982) 3894.
[9] S. Giri, K. Ghoshray, Phys. Rev. B 57 (1998) 5918.
[10] A. Caramanian, N. Dupont, P. Gredin, A. de Kozak, Z. Anorg. Allg. Chem. 625 (1999) 933.
[11] S. Siegel, Acta Crystallogr. 9 (1856) 684.
[12] E. Ehrlich, G. Pictzka, Z. Anorg. Allg. Chem. 275 (1954) 121.
[13] R. Hoppe, S. Becker, Z. Anorg. Allg. Chem. 568 (1989) 126.
[14] St. Becker, R. Hoppe, Z. Anorg. Allg. Chem. 579 (1989) 16.
[15] A.K. Tyagi, R. Pottgen, J. Kohler, Z. Anorg. Allg. Chem. 622 (1996) 1329.
[16] M. Dadachov, L. Eriksson, Acta Crystallogr. C55 (1999) 1739.
[17] S. Yamanaka, A. Yasuda, H. Miyata, J. Solid State Chem. 183 (2010) 256.
[18] R.A. Laudise, J. Am. Chem. Soc. 81 (1958) 562.
[19] R.A. Laudise, A.A. Ballman, J. Am. Chem. Soc. 80 (1958) 2655.
[20] D.W. Breck, Zeolite Molecule Sieves: Structure, Chemistry and Use, Wiley and Sons, London, 1974.
[21] R.M. Barrer, Hydrothermal Chemistry of Zeolites, Academic Press, London, 1982.
[22] R. Szostak, Molecular Sieves: Principles of Synthesis and Identification, Reinhold, New York, 1989.
[23] SAINT, Program for Area Detector Absorption Correction, Version 4.05; Siemens Analytical X-ray Instruments: Madison, WI, USA, 1995.
[24] R.H. Blessing, Acta Crystallogr. A51 (1995) 33.
[25] G.M. Sheldrick, SHELXS-97—A Program for Automatic Solution of Crystal Structures, University of Goettingen, Goettingen, Germany, 1997.

[26] G.M. Sheldrick, SHELXL-97—A Program for Crystal Structure Refinement, University of Goettingen: Goettingen, Germany, 1997.
[27] L.J. Farrugia, J. Appl. Crystallogr. 32 (1999) 837.
[28] P. Kubelka, F. Munk, Z. Tech. Phys. 12 (1931) 593.
[29] J. Tauc, Mater. Res. Bull. 5 (1970) 721.
[30] G. Kresse, D. Joubert, Phys. Rev. B 59 (1999) 1758.
[31] G. Kresse, J. Furthmüller, Vienna Ab-initio Simulation Package (VASP); Computational Physics, Faculty of Physics, Universität Wien: Wien, Austria, 2004; 〈http://cms.mpi.univie.ac.at/vasp〉.
[32] J.P. Perdew, K. Burke, M. Ernzerhof, Phys. Rev. Lett. 77 (1996) 3865.
[33] I. Pastoriza-Santos, L.M. Liz-Marzan, Adv. Funct. Mater. 19 (2009) 679.
[34] J.Y. Yu, S. Schreiner, L. Vaska, Inorg. Chim. Acta 170 (1990) 145.
[35] D.R. Sears, J.L. Hoard, J. Chem. Phys. 50 (1969) 1066.
[36] B. Bersucker, Coord. Chem. Rev. 14 (1975) 357.
[37] I.D. Brown, D. Altermatt, Acta Crystallogr. B41 (1985) 244.
[38] N.E. Brese, M. O'Keeffe, Acta Crystallogr. B47 (1991) 192.
[39] I.R. Beattie, P.J. Jones, J. Chem. Phys. 90 (1989) 5209.
[40] N.M. Laptash, J. Fluorine Chem. 105 (2000) 59.